# Experimental and Computational Steady and Unsteady Transonic Flows about a Thick Airfoil

Lionel L. Levy Jr.*
*NASA Ames Research Center, Moffett Field, Calif.*

**An experimental and computational investigation of the steady and unsteady transonic flowfields about a thick airfoil is described. An operational computer code for solving the two-dimensional, compressible Navier-Stokes equations for flow over airfoils was modified to include solid-wall, slip-flow boundary conditions to properly assess the code and help guide the development of improved turbulence models. Steady and unsteady flowfields about an 18% thick circular arc airfoil at Mach numbers of 0.720, 0.754, and 0.783 and a chord Reynolds number of $11\times10^6$ are predicted and compared with experiment. Results from comparisons with experimental pressure and skin-friction distributions show improved agreement when including test-section wall boundaries in the computations. Steady-flow results were in good quantitative agreement with experimental data for flow conditions which result in relatively small regions of separated flow. For flows with larger regions of separated flow, improvements in turbulence modeling are required before good agreement with experiment will be obtained. For the first time, computed results for unsteady turbulent flows with separation caused by a shock wave were obtained which qualitatively reproduce the time-dependent aspects of experiments. Features such as the intensity and reduced frequency of airfoil surface-pressure fluctuations, oscillatory regions of trailing-edge and shock-induced separation, and the Mach number range for unsteady flows were all qualitatively reproduced.**

## Nomenclature

| | |
|---|---|
| A | = Van Driest damping length |
| $c_f$ | = skin-friction coefficient, $\tau_w/q_\infty$ |
| $C_p$ | = pressure coefficient $(p_w-p)/q_\infty$ |
| $c$ | = airfoil chord |
| $e$ | = internal energy |
| $\bar{f}$ | = reduced frequency, $2\pi$ (frequency) $(c/2)/u_\infty$ |
| $\ell$ | = mixing length of turbulence |
| $M$ | = Mach number |
| $n,t$ | = local coordinates normal and tangential to test-section wall |
| $\Delta n$ | = normal distance between image point and test-section wall |
| $p$ | = pressure |
| $p_t$ | = total pressure |
| $\Delta p$ | = instantaneous $p$—mean value of $p$ |
| $q$ | = total velocity, $(u^2+v^2)^{1/2}$ |
| $q_\infty$ | = freestream dynamic pressure, $(\frac{1}{2})\rho_\infty u_\infty^2$ |
| $R$ | = radius of curvature |
| $Re_{c,\infty}$ | = chord Reynolds number, $\rho_\infty u_\infty c/\mu_\infty$ |
| $T$ | = temperature |
| $t$ | = time |
| $u,v$ | = velocity components in $x$ and $y$ directions, respectively |
| $x,y$ | = axes parallel and normal, repectively, to airfoil chord with origin at airfoil leading edge |
| $y_{DS}$ | = location of separation streamline |
| $\gamma$ | = ratio of specific heats |
| $\delta$ | = thickness of viscous region |
| $\epsilon$ | = eddy viscosity coefficient |
| $\mu$ | = molecular viscosity |
| $\tau$ | = shear stress |
| $\psi$ | = angle whose tangent is the local slope of the test-section wall |

*Subscripts*

| | |
|---|---|
| $b$ | = wall boundary point outside of test section |
| $i$ | = image point inside of test section |
| $\infty$ | = freestream value |
| $n,t$ | = components normal and tangential to test-section wall |
| $w$ | = airfoil surface or test-section wall |
| $\delta$ | = value at outer edge of viscous region |

Presented as Paper 77-678 at the AIAA 10th Fluid and Plasmadynamics Conference, Albuquerque, N. Mex., June 27-29, 1977; submitted June 27, 1977; revision received Jan. 27, 1978. 

Index categories: Computational Methods; Nonsteady Aerodynamics; Transonic Flow.

*Research Scientist. Member AIAA.

## I. Introduction

THE NASA Ames Research Center has initiated combined research programs in experimental and computational fluid dynamics for testing and guiding the development of turbulence modeling within regions of separated flows.[1] Toward this end, the flowfield about an 18% thick circular arc airfoil is being experimentally documented over a range of Mach and Reynolds numbers for which the major features of flow separation important to turbulence modeling are present, including weak and strong shock-wave boundary-layer interactions and both trailing-edge and shock-induced boundary-layer separation. Results to date for pressure and skin-friction distributions have beem compared in Refs. 2 and 3, respectively, with computed results from a two-dimensional code for time-dependent solutions of Reynolds-averaged, compressible Navier-Stokes equations.[4] The computer code includes additional equations for turbulence modeling and applies only to free-flight conditions; it does not include test-section wall boundary conditions. Consequently, comparisons of experimental and computed results made in Refs. 2 and 3 are considered to show qualitatively correct trends. Before different turbulence models can be quantitatively tested against the pressure and skin-friction data from these references, the proper outer wall boundary conditions must be incorporated into the computer code.

This paper describes the modifications to the computer code of Refs. 4 and 5 to include solid-wall inviscid boundary conditions. Results are presented which show differences in pressure and skin-friction distributions over an 18% thick circular arc airfoil, calculated by using free-flight boundary conditions and the solid-wall test-section boundaries of the experiments reported in Refs. 2 and 3. Experimental results are included for comparison.

As reported in Ref. 2, both steady and unsteady flows were observed for specific ranges of freestream Mach numbers and chord Reynolds numbers. For example, for a given chord Reynolds number, there was observed a low subsonic Mach number range (above that for locally sonic flow on the airfoil) and a high subsonic Mach number range for which the local flowfield was steady. In the intermediate Mach number range, the local flowfield was unsteady and periodic.

The original intent in applying the modified computer code with wall boundary conditions was to obtain a solution for comparison with experiment at freestream conditions within each steady-flow regime near the boundaries of the unsteady-flow regime. As noted in Ref. 2, definition of the low Mach number boundary of the unsteady-flow regime is subject to hysteresis in the flowfield. The initial selection of freestream conditions for a solution in the low Mach number steady-flow regime was inadvertently made in the region of hysteresis. Surprisingly, an unsteady flowfield solution was obtained. The results are included in this paper and demonstrate, for the first time, the capabilities of the computer code to reproduce qualitatively the time-dependent aspects of experimentally observed unsteady turbulent flows with both weak and strong shock-wave boundary-layer interactions. Features important to airplane buffet such as oscillations in shock-wave location and strength and alternate regions of trailing-edge and shock-induced boundary-layer separation are reproduced.

## II. Analysis

### Simulation Method

The transonic flowfield about the airfoil was simulated numerically using a form of the computer program described in Ref. 5. The program utilizes an explicit finite-difference method[6-8] to solve the time-dependent, two-dimensional, Reynolds averaged form of the Navier-Stokes equations applicable to compressible turublent flows. The turbulence is assumed in equilibrium with the mean flow and is modeled using an algebraically expressed eddy viscosity model. The computer program also incorporates the efficient numerical solver for Navier-Stokes equations described in Ref. 9. The flow and turbulence-modeling equations are repeated here for completeness.

The flow equations in time-dependent form are

$$\frac{\partial}{\partial t}\int_{\text{vol}} U\,\mathrm{d}\,\text{vol} + \int_s \vec{H}\cdot\vec{n}\,\mathrm{d}s = 0$$

where

$$U \equiv \begin{Bmatrix} \rho \\ \rho u \\ \rho v \\ e \end{Bmatrix} \qquad \vec{H} \equiv \begin{Bmatrix} \rho\vec{q} \\ \rho u\vec{q} + \vec{\tau}\cdot\vec{e}_x \\ \rho v\vec{q} + \vec{\tau}\cdot\vec{e}_y \\ e\vec{q} + \vec{\tau}\cdot\vec{q} - k\nabla T \end{Bmatrix}$$

$$\vec{q} \equiv u\vec{e}_x + v\vec{e}_y$$

$$\vec{\tau} \equiv \sigma_x\vec{e}_x\vec{e}_x + \tau_{xy}\vec{e}_x\vec{e}_y + \tau_{yx}\vec{e}_y\vec{e}_x + \sigma_y\vec{e}_y\vec{e}_y$$

The quantities $\sigma_x$ and $\sigma_y$ are the normal stresses in the $x$ and $y$ directions, respectively, $\vec{e}_x$, $\vec{e}_y$ are unit vectors in orthogonal $x,y$ space, and $\vec{n}$ is a unit normal vector to the surface element $ds$ about the volume element vol.

The turbulence modeling is incorporated in the shear stress terms $\tau_{xy}$ and $\tau_{yx}$ in the form of an eddy viscosity coefficient $\epsilon$ as

$$\tau = \tau_{xy} = \tau_{yx} = (\mu + \rho\epsilon)[(\partial u/\partial y) + (\partial v/\partial x)]$$

Expressions for the eddy viscosity coefficient in the regions of the boundary layer and wake indicated in Fig. 1 are listed below.

Inner region (I)

$$\epsilon = \ell^2\left[\left(\frac{\partial u}{\partial y}\right)^2 + \left(\frac{\partial v}{\partial x}\right)^2\right]^{1/2}$$

$$\ell = 0.41y[1 - \exp(-y/A)]$$

where the Van Driest damping length is

$$A = 26\frac{\mu_w}{\rho_w}\left(\frac{\rho_w}{|\tau_w|}\right)^{1/2}$$

Outer region (II) of boundary layer and wake

$$\epsilon = \ell^2\left[\left(\frac{\partial u}{\partial y}\right)^2 + \left(\frac{\partial v}{\partial x}\right)^2\right]^{1/2}$$

$$\ell = 0.09(y_\delta - y_{DS})$$

In region II over the separated bubble (regions III and IV), $\ell$ is frozen at the value evaluated at the first computational chordwise station upstream of separation.

Separation bubble wall region (III)

$$\rho\epsilon = (\rho\epsilon)_{DS}\left(\frac{y - y_w}{y_{DS} - y_w}\right)$$

Separation bubble wake region (IV)

$$\rho\epsilon = (\rho\epsilon)_{DS}$$

The control volume, mesh, and boundary conditions are described in detail in Ref. 5. Briefly, the airfoil, initially at rest, is impulsively started at time zero at the desired freestream Mach number and pressure. The control volume, $-12$ and $+8$ chords in the $x$ direction and $\pm 6$ chords in the $y$ direction, is divided into a $78\times 35$ mesh. The flowfield development within this volume is followed in time until it attains a steady state. For the present code, airfoil, and freestream conditions, this requires a time equivalent to the mean flow traveling about 9 chord lengths past the airfoil ($u_\infty t/c = 9$). At the far upstream and transverse boundaries, the flow is assumed uniform and at freestream conditions. At the downstream boundary, all gradients in the flow direction are assumed negligible. The airfoil is assumed impermeable (no-slip boundary conditions) and adiabatic, and the pressure gradient normal to the surface is assumed zero.

### Modifications to Include Tunnel-Wall Boundary Conditions

Use of the experimental data of Refs. 2 and 3 to assess existing turbulence models and help develop improved models necessitated the choice of solid-wall boundary conditions. Computer storage and time significantly influenced the decision that the initial effort be based upon inviscid slip-flow boundary conditions.

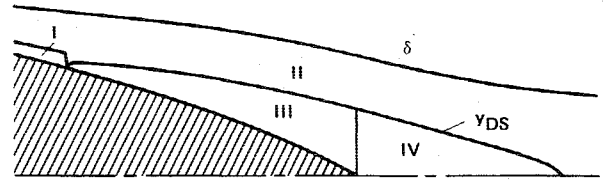


**Fig. 1 Boundary-layer and wake regions for turbulence model.**

To minimize the modifications, the wall boundaries are superimposed upon the computational mesh used to obtain free-flight solutions. Computations with the walls are made for the entire mesh. However, at each of the computational mesh points just outside the wall boundaries, the dependent variables (horizontal and vertical components of velocity, internal energy, and pressure) are updated at each time step to satisfy the inviscid boundary conditions. This procedure is only slightly inefficient, since approximately 90% of the computational time is used in resolving the airfoil boundary-layer flow. Inclusion of the wall boundaries results in an 8% increase in computer time over that required for a free-flight solution.

In the present approach the coordinates, slope, and local wall curvature of the test section studied are used as inputs to the modified computer program. The program then finds all computational mesh points (mesh centroids) just outside the boundaries. Next, the image points of these boundary centroids are constructed normal to and inside the test section flowfield. Values of the dependent variables at the mesh points in the flowfield which most closely surround each image point are used for interpolation to obtain values of the dependent variables at the image points. These values of the dependent variables, at each time step, are used in conjunction with boundary conditions to continually update the dependent variables at the boundary centroids. Specifically, the horizontal and vertical components of velocity at the boundary points, $u_b$ and $v_b$, respectively, are determined such that, locally, the total velocity $q$ is tangent to the walls (i.e., no flow through the walls). With reference to Fig. 2 these conditions are written

$$q_{t_b} = q_{t_i} = q_{t_w} \tag{1}$$

$$q_{n_b} = -q_{n_i}; \quad q_{n_w} = 0 \tag{2}$$

From Eqs. (1) and (2) and the slope of the wall, it can be shown that

$$u_b = u_i(\cos^2\psi - \sin^2\psi) + 2v_i \sin\psi \cos\psi \tag{3}$$

$$v_b = 2u_i \sin\psi \cos\psi - v_i(\cos^2\psi - \sin^2\psi) \tag{4}$$

The internal energy $e_b$ at each boundary point is readily determined using the assumption of an adiabatic wall. Thus,

$$e_b = e_i = e_w \tag{5}$$

The pressure $p_b$ at the boundary points is determined from the normal momentum equation

$$\left(\frac{\partial p}{\partial n}\right)_w = -\frac{\rho_w q_{t_w}^2}{R_w} \tag{6}$$

Equation (6) can be rewritten by discretizing the partial derivative, making use of the equation of state, and expressing $q_{t_w}$ as a function of the known quantities, $u_i$, $v_i$, and $\psi$:

$$\frac{p_w - p_i}{n_w - n_i} = \frac{p_w - p_i}{\Delta n} = -\frac{(u_i\cos\psi + v_i\sin\psi)^2}{(\gamma - 1)e_w R_w} p_w \tag{7}$$

Finally, by assuming that $p_w = \frac{1}{2}(p_b + p_i)$, and with use of Eq. (5), the pressure at each boundary centroid is given by

$$p_b = \frac{1 - B}{1 + B} p_i \tag{8}$$

where

$$B = \frac{\Delta n(u_i\cos\psi + v_i\sin\psi)^2}{(\gamma - 1)e_i R_w} \tag{9}$$

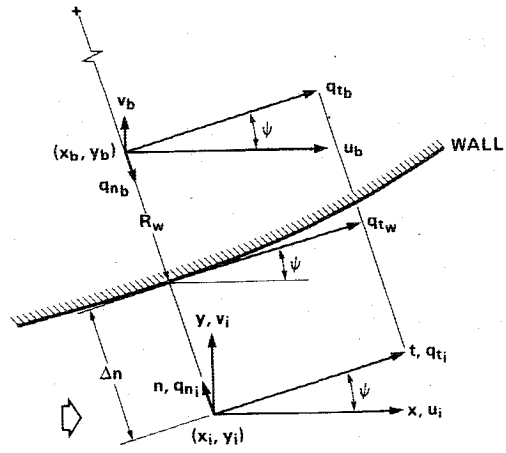


**Fig. 2 Flowfield and geometrical relationships for wall boundary conditions.**

and

$$\Delta n = (y_b - y_i)/2\cos\psi \tag{10}$$

To verify that the numerical algorithm for the wall boundary conditions was correct, two streamlines from a solution of a lifting airfoil in free flight were selected as upper and lower "walls" of a test channel. A solution was then obtained at identical freestream conditions for the airfoil in the presence of these walls. Within the accuracy of the numerical method, the flowfield about the airfoil should be the same for both solutions. This is demonstrated to be the case by the pressure distributions on the airfoil surfaces and along the free-flight streamlines and channel walls shown in Fig. 3.

## III. Results and Discussion

The upper and lower test-section walls used in the experiments reported in Refs. 2 and 3 were contoured to the shape of streamlines computed using an inviscid code. Streamlines used were one-half of the channel height away from the chordline of an 18% thick circular arc airfoil at a freestream Mach number $M_\infty$ of 0.775. These walls were diverged slightly to compensate for channel-wall boundary-layer growth and were unchanged for tests at all Mach and Reynolds numbers. Thus, many of the experimental data of Refs. 2 and 3 were obtained at off-design conditions. Consequently, use of these experimental data to test the validity of turbulence modeling requires that the computer code contain the boundary conditions of the experiment. The actual wall coordinates of the experimental apparatus were used. All subsequent results are for an 18% thick circular arc airfoil at 0 deg angle of attack, and only results for half the flowfield are presented (with the exception of computed Mach contours of the entire flowfield). To avoid numerical difficulties, all computed results were obtained for an 18% thick circular arc airfoil with 1% chord nose radius.

### Computed Effect of Wall Boundaries

Figure 4 shows the actual channel walls and streamlines, through the beginning of the contoured portion of the walls, obtained from free-flight viscous solutions at $M_\infty = 0.783$ and 0.720 and a chord Reynolds number $Re_{c,\infty}$ of $11 \times 10^6$. Note that an expanded ordinate is used to emphasize the wall and streamline shapes. The channel walls are a reasonable representation of the streamlines from the $M_\infty = 0.783$, $Re_{c,\infty} = 11 \times 10^6$ solution. Consequently, these freestream conditions constitute a near-design test condition, and the results in Fig. 5 for free-flight and wall boundary conditions demonstrate that the respective differences between pressure and skin-friction distributions are small. Comparison of

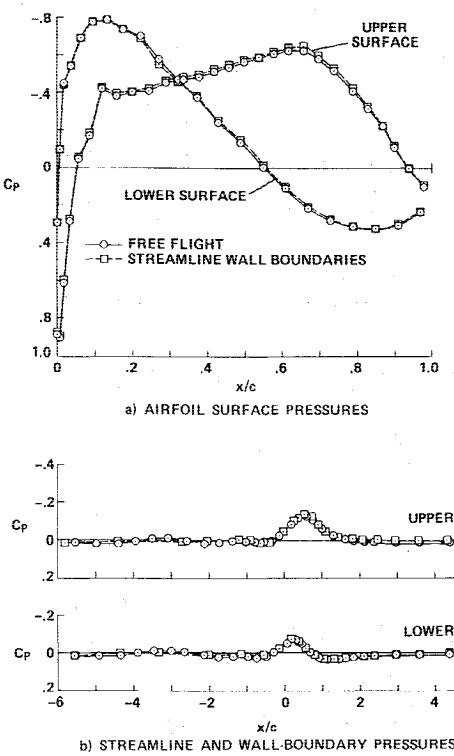


**Fig. 3 Calculated pressure distributions for a lifting airfoil in free flight and in a test channel with walls contoured to the shape of free-flight streamlines; Korn-Garabedian airfoil, $M_\infty = 0.756$, $Re_{c,\infty} = 21 \times 10^6$, $\alpha = -1.54$ deg.**

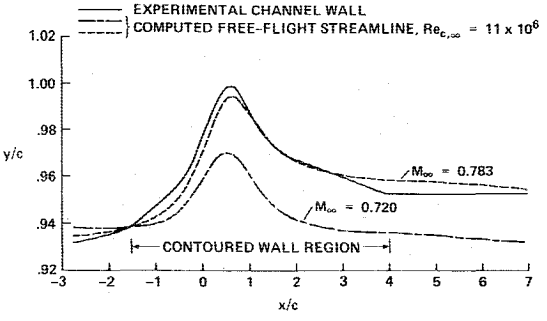


**Fig. 4 Channel wall and streamlines through beginning coordinate of wall for the 18% thick circular arc airfoil, $\alpha = 0$ deg.**

either set of computed results in Fig. 5 with experiment to assess the adequacy of the computer code and turbulence model would lead to essentially the same conclusions for this near-design case.

For the off-design conditions of $M_\infty = 0.720$ and $Re_{c,\infty} = 11 \times 10^6$, the results in Fig. 4 show that the actual channel walls provide more "open area" about the airfoil than would exist had the walls been contoured to the shape of streamlines obtained from the free-flight viscous solution. Consequently, compared to free-flight results, the pressure field computed about the airfoil would be less severe when including the actual channel-wall boundaries. This is demonstrated by the computed pressure and skin-friction distributions shown in Fig. 6. These results indicate the necessity for a computer code with proper boundary conditions when using experimental results to assess the adequacy of a code and turbulence model. Obviously, comparisons at off-design conditions between experimental data and solutions with channel walls would lead to a different assessment of the code and turbulence model than would similar computations using free-flight boundary conditions.

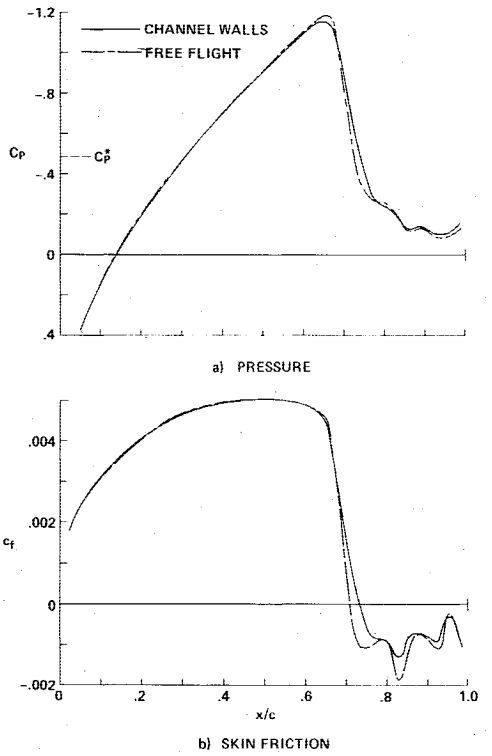


**Fig. 5 Computed pressure and skin-friction distributions on the circular arc airfoil with free-flight and channel wall boundary conditions, $M_\infty = 0.783$, $Re_{c,\infty} = 11 \times 10^6$, $\alpha = 0$ deg.**

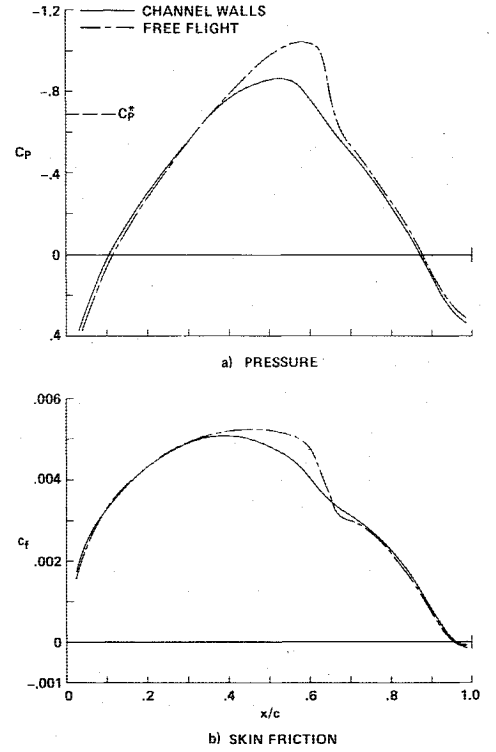


**Fig. 6 Computed pressure and skin-friction distributions on the circular arc airfoil with free-flight and channel wall boundary conditions, $M_\infty = 0.0720$, $Re_{c,\infty} = 11 \times 10^6$ $\alpha = 0$ deg.**

### Comparisons with Experiment

As noted in the Introduction, during the experiments reported in Ref. 2 both steady and unsteady flows were observed for specific ranges of freestream Mach numbers and chord Reynolds numbers. Figure 7 has been reproduced from

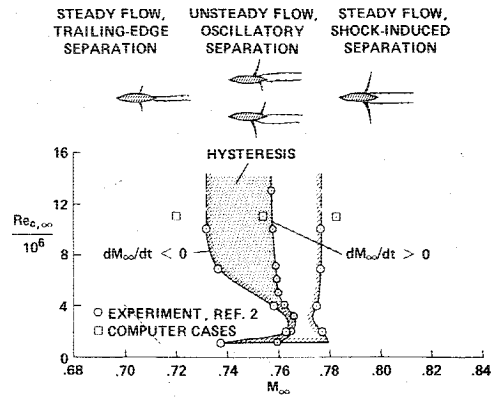


**Fig. 7 Experimental flow domains for the 18% thick circular arc airfoil.**

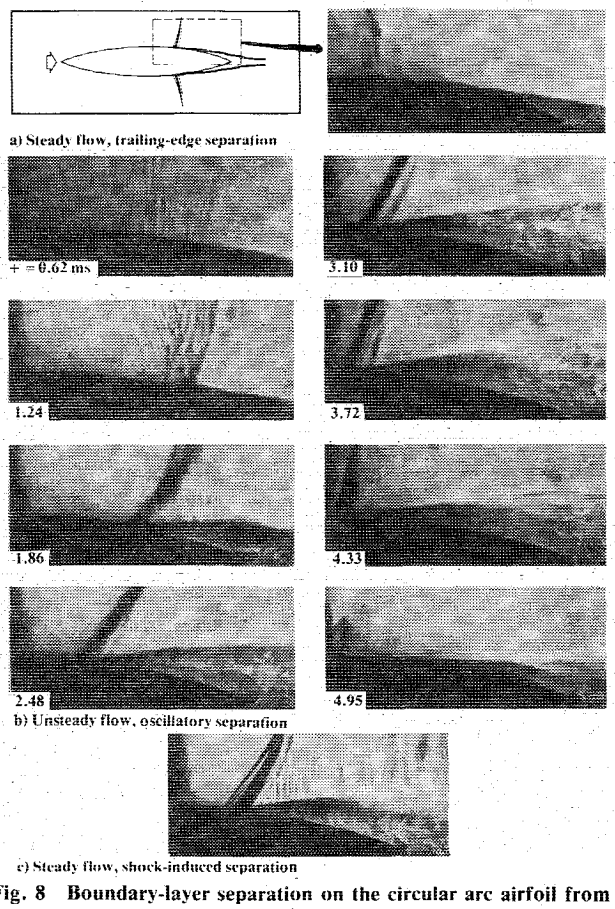


**Fig. 8 Boundary-layer separation on the circular arc airfoil from a shadowgraph movie.**

Ref. 2 to identify the Reynolds number and Mach number domains within which three distinctively different types of flow have been documented for the 18% thick circular arc airfoil. The steady flow in the low Mach number domain was characterized by a weak shock wave near midchord and trailing-edge boundary-layer separation. This flow picture is depicted by the left-most sketch in Fig. 7. A more detailed picture of the trailing edge is illustrated by a selected frame from a shadowgraph movie, reproduced from Ref. 10, in Fig. 8a. The unsteady flow domain shown in Fig. 7 includes the region of flow hysteresis in the lower Mach number range noted earlier. The flow in this domain was characterized by periodic oscillations in shock-wave location and intensity and concomitant oscillations between trailing-edge and shock-induced separation of the boundary layer. This flow phenomenon is depicted by the middle sketches in Fig. 7 and

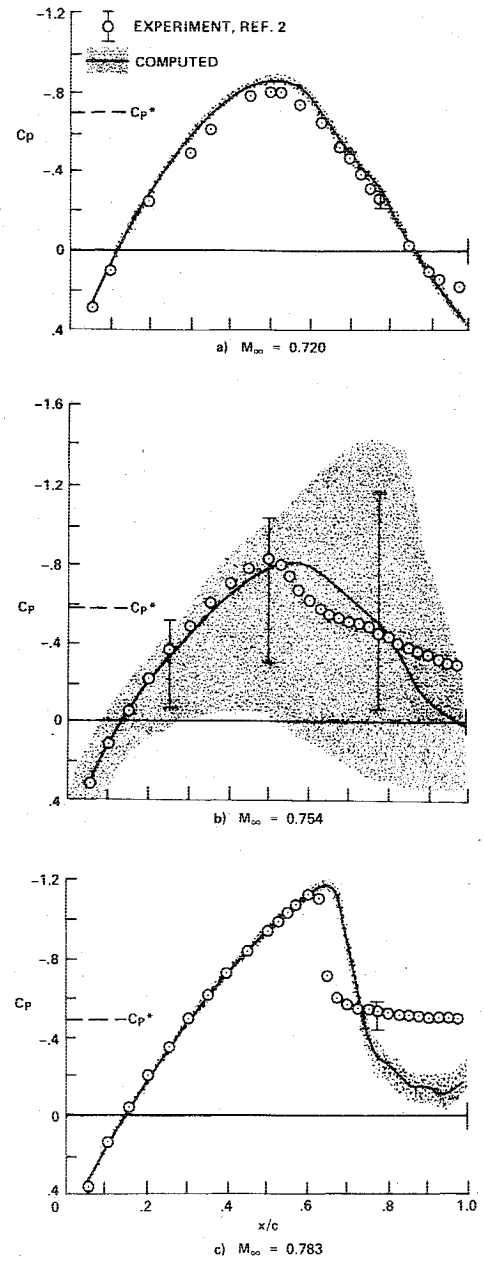


**Fig. 9 Computed and experimental pressure distributions on the circular arc airfoil, $Re_{c,\infty} = 11 \times 10^6$.**

the movie frames in Fig. 8b. In the high Mach number, steady-flow domain, a shock wave occurs near the 70% chord station sufficiently strong to induce boundary-layer separation at the base of the shock wave; see the right-most sketch in Fig. 7 and movie frame in Fig. 8c. Indicated by the square symbols in Fig. 7 are three sets of freestream conditions, $M_\infty = 0.720, 0.754, 0.783$ and $Re_{c,\infty} = 11 \times 10^6$, one in each flow domain, for which computer solutions with wall boundaries have been obtained for comparisons with available experimental data.

The flowfields in the two steady flow domains, in actuality, are pseudo-steady. Specifically, the shock-wave location and intensity, the point of boundary-layer separation, and the pressure and skin-friction distributions do experience small excursions about respective mean values in both the experiment and the computations. The amplitudes of these excursions are an order of magnitude or more smaller than in the unsteady flow domain. This will become apparent in discussions of subsequent results.

Experimental pressure distributions from Ref. 2 and the present computed results are shown in Fig. 9 for the three sets

of freestream conditions just noted. The symbols denote the mean values of the experiment, and the bars on the symbols at $x/c = 0.25$, 0.50, and 0.775 represent maximum and minimum values of fluctuations about the mean; they do not denote the uncertainty of the measured mean values. (The pressure fluctuations at $x/c = 0.25$ were obtained by McDevitt.[13]) Mean values from the computations are denoted by the solid lines and the range of fluctuations by the shaded areas. For the steady-flow cases at $M_\infty = 0.720$ and 0.783, Figs. 9a and 9c, respectively, the computed mean values are the averages over a time equivalent to several chord lengths of mean flow travel beyond that for which the solution is normally considered to have converged to a steady state. Computed results for the unsteady-flow case at $M_\infty = 0.754$, Fig. 9b, are from time histories of four consecutive cycles of flowfield oscillation (approximately 32 chord lengths).

The steady flowfield at $M_\infty = 0.720$ is characterized by a weak shock wave and trailing-edge separation (see Figs. 7 and 8a). The computed results in Fig. 9a are in good agreement with experiment over most of the airfoil. Failure of these results to better predict the pressures in the separated region near the trailing edge is attributed to inadequate turbulence modeling in this region. The amplitudes of the measured pressure fluctuations at $x/c = 0.25$ and 0.50 lie within the symbols and are not shown. The mean results for the computations shown in Fig. 9a are the same results shown in Fig. 6a for the channel walls. A comparision of the computed free-flight pressure distribution shown in Fig. 6a with the experimental data in Fig. 9a would indicate poor agreement in the range $0.45 < x/c < 0.70$. In this case, one would erroneously suspect deficiencies in the computer code and/or turbulence model. The results of these contrasting comparisons emphasize the necessity for computer codes with the proper boundary conditions.

The steady flowfield at $M_\infty = 0.783$ is characterized by a strong shock wave and shock-induced separation (see Figs. 7 and 9c). The computed results in Fig. 9c (and Fig. 5a) are in excellent agreement with experiment ahead of the shock wave ($x/c = 0.675$). The large differences between the computed and experimental mean results in the region of the shock wave and aft in the region of shock-induced separation again are attributed to inadequate turbulence modeling. In the separated region at $x/c = 0.775$, it is interesting to note the good agreement between the computed and measured magnitudes of the pressure fluctuations. Here, also, the fluctuation magnitudes at $x/c = 0.25$ and 0.50 are within the symbols.

The unsteady flowfield at $M_\infty = 0.754$ is characterized by periodic shock-wave oscillations and oscillations in boundary-layer separation between the trailing-edge and shock-induced type (see Figs. 7 and 8b). The calculated and experimental mean pressures agree well over the forward half of the airfoil. The similarity in the trends of the variation of the magnitude of pressure fluctuations about the mean value strongly suggests the possibility that the wave form of the experimental pressure fluctuations also may be reproduced by the calculations. This is shown to be the case in Fig. 10. Experimental and computed time histories of the instantaneous pressure oscillations about the mean pressure (normalized by the channel total pressure) on the upper and lower airfoil surfaces at two chord stations are reproduced from Ref. 10. The qualitative agreement between the different wave forms at two chordwise stations is surprisingly good considering that the computed unsteady results were obtained using simple algebraic eddy viscosity to model turbulence. The 180-deg phase difference between the dynamic pressures on upper and lower airfoil surfaces at identical chord stations demonstrate that the oscillatory unsteadiness is an asymmetric phenomenon, both in the experiment and in the computations. The reduced frequency of the surface pressure oscillations determined from the numerical solution, $\bar{f} = 0.40$, differs from that reported in Ref. 2 ($\bar{f} = 0.49$) only by about 20%.

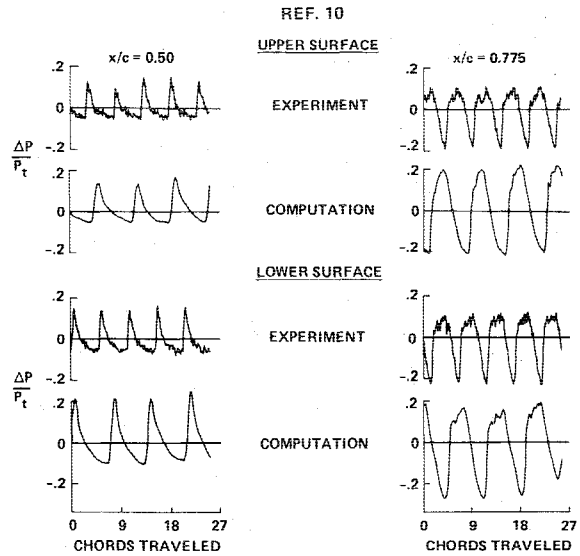


**Fig. 10 Computed and experimental surface-pressure time histories on the circular arc airfoil, $M_\infty = 0.754$, $Re_{c,\infty} = 11 \times 10^6$.**

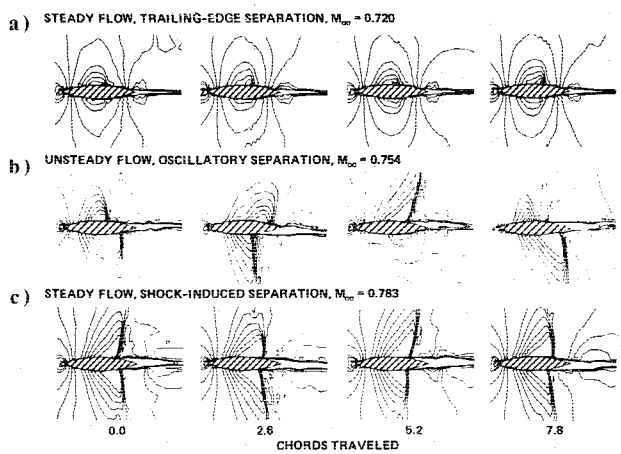


**Fig. 11 Mach contours in the flow field about the circular arc airfoil from a computer movie.**

Further evidence that Navier-Stokes type computer codes with simple turbulence models reproduce shock-wave and boundary-layer spearation features for steady flows and are capable of qualitatively reproducing the time-dependent aspects of these features for unsteady flows is presented in Fig. 11. Selected frames illustrating the three distinctively different types of flow just discussed are reproduced from a computer movie of Mach contours. The elapsed time corresponds to the chord lengths traveled by the mean flow during one cycle of the oscillatory flow shown in Fig. 11b. Coalescence of the near-vertical contours over the latter half of the airfoil indicates the formation of a shock wave—the closer the contours, the stronger the shock wave. The horizontal contours aft of the shock waves and in the wake are in the outer region of the boundary layer and wake denoted as region II in Fig. 1.

A careful comparison of Fig. 11 with the shadowgraphs in Fig. 8 reveals marked similarities between the computed and experimental flowfield features for both steady and unsteady flows. Figures 8a and 11a depict steady flow with a weak shock wave and trailing-edge separation. Figures 8c and 11c show a strong shock wave with a large region of flow separation emanating from the base of the shock wave. The flow similarities between Figs. 8b and 11b for the unsteady-flow case further demonstrate that the oscillatory unsteadiness is an asymmetric phenomenon. For example, the

shock wave forms near the trailing edge just above a region of trailing-edge separation (note the upper surface in the second frame in Fig. 11b and the $t=0.62$ ms frame in Fig. 8b). The shock wave increases in strength as the local airfoil surface velocities ahead of the shock increase. The increased strength gives rise to shock-induced separation, and the shock wave and separated region begin to move forward. The local surface velocities upstream of the shock continue to increase and stabilize in a maximum velocity distribution. As the shock continues forward into a region of locally lower velocities, it diminishes in strength and vanishes as the separation point reverts to the trailing edge to complete the cycle. Meanwhile, the identical process is occurring on the lower surface 180 deg out of phase.

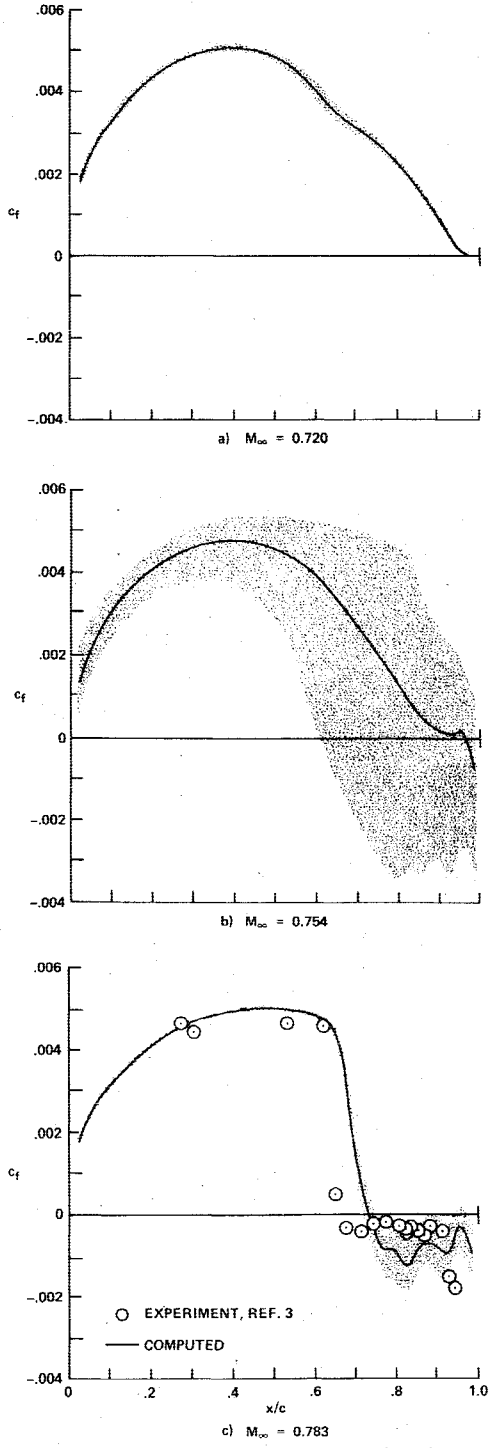


**Fig. 12 Computed and experimental skin-friction distributions on the circular arc airfoil, $Re_{c,\infty}=11\times10^6$.**

Computed and experimental skin-friction distributions are shown in Fig. 12 for the three flow conditions of interest. The computed results were obtained from the same sets of flowfield data described earlier in discussing the pressure distributions. It is not surprising, therefore, that the trends in the computed magnitudes of the skin-friction fluctuations (shaded areas) about the mean values (solid lines) are similar to those noted for the pressure fluctuations. Experimental data are available from Ref. 3 only for $M_\infty=0.783$. The distribution of mean values of skin friction is shown in Fig. 12c. As in the case of the pressure distribution (see Fig. 9c), the agreement between the computed and measured values is good ahead of the shock wave. The poor agreement in defining the shock-wave location and aft in the separated-flow region is again attributed to deficiencies in the turbulence model.

As discussed in Ref. 3, the skin-friction gages used respond to a skin-friction parameter which is a combination of the flow quantities $\mu_w\rho_w\tau_w$. Because fluctuating pressure measurements were not recorded simultaneously with the fluctuating skin-friction data, it was not possible to determine the magnitudes of the maximum and minimum excursions in skin friction from dynamic records of $\mu_w\rho_w\tau_w(\rho_w\sim p_w)$. Therefore, only the calculated and experimentally deduced values of the root-mean-square variations in the unsteady skin-friction parameter are compared here. The rms values shown in Fig. 13 have been normalized by a value near the midchord ahead of the shock wave. The sign of the ordinate in Fig. 13 corresponds to that of the local mean value of the skin friction. Just as these results for mean skin-friction show, the computed unsteady skin-friction results indicate the shock to be further downstream than in the experiment. However, the trends showing a rapid increase in dynamic activity ahead of the shock wave and an increased magnitude in the fluctuations downstream in the shock-induced separation region are similar.

The present results comprise a substantial amount of circumstantial evidence which indicates, for the first time, that Navier-Stokes type computer codes are capable of reproducing the time-dependent aspects of experimentally documented unsteady turbulent flows with shock-induced separation. However, just as the experimenter always questions whether unsteady flows are caused by some resonant tunnel phenomena, so the numerical analyst naturally inquires if computed unsteady-flow results are caused by the wall boundary conditions, numerical inaccuracies, or computer-code asymmetries. The experimenter demonstrates that the unsteady flow is aerodynamically induced by using records of the aerodynamically different airfoil and wind-tunnel frequencies (see, e.g., Refs. 2 and 11) and by testing airfoils of different chord lengths and observing a constant airfoil reduced frequency (see, e.g., Refs. 11 and 12). The numerical analyst can make similar

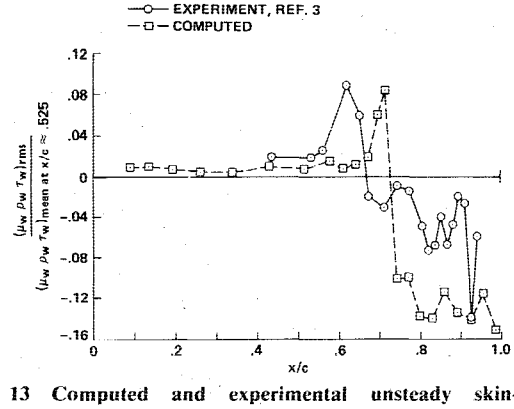


**Fig. 13 Computed and experimental unsteady skin-friction parameters for the circular arc airfoil, $M_\infty=0.783$, $Re_{c,\infty}=11\times10^6$.**

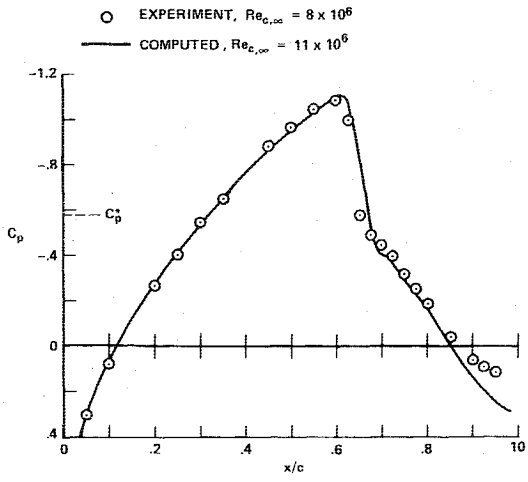


**Fig. 14 Computed and experimental pressure distributions on the circular arc airfoil with a quarter-chord trailing-edge splitter plate, $M_\infty = 0.754$.**

demonstrations in addition to checks for numerical accuracy and asymmetry.

The computed unsteady flows were determined not to have been induced by including the channel walls as boundary conditions. This was determined from the results of a solution for the present airfoil at $M_\infty = 0.754$ and $Re_{c,\infty} = 11 \times 10^6$ in free flight. A periodic unsteady-flow solution was obtained. The reduced frequency and magnitudes of the airfoil surface pressure oscillations were slightly different from similar results for the solution including the channel walls and did not agree as well with experiment. Similar to the approach taken in Refs. 11 and 12, a solution with wall boundaries was obtained at the present unsteady-flow free-stream conditions for the same airfoil with one-half the present chord. An unsteady-flow solution was obtained and the frequency of the airfoil surface pressure oscillations was twice that for the longer chord airfoil; thus the reduced frequency was constant at $\bar{f} = 0.40$.

A cursory investigation of the unsteady-flow solutions has revealed that they are, in fact, a result of viscous phenomena and not a result of numerical inaccuracies. For example, inviscid computations for the same $M_\infty$ produced a steady-flow solution. A viscous solution for a half airfoil at $M_\infty = 0.754$ and $Re_{c,\infty} = 11 \times 10^6$ produced a steady-flow solution. The half-model boundary conditions, however, preclude communication of pressure waves across the airfoil wake and provide a solid boundary upon which the separated boundary layer can reattach. A similar, more physically realistic test is to experimentally and computationally reduce such communication across the wake and provide a solid boundary by using a trailing-edge splitter plate of sufficient length to produce a steady flow. It was determined experimentally that a one-quarter-chord trailing-edge splitter plate stopped the unsteady flow at all Reynolds numbers for which unsteady flow occurred without the splitter plate at $M_\infty = 0.754$ (see Fig. 7).[13] Viscous computations for the same airfoil and splitter plate at $M_\infty = 0.754$ and $Re_{c,\infty} = 11 \times 10^6$ produced a steady-flow solution. The computed and experimental airfoil pressure distributions are shown in Fig. 14.[13] The agreement is very good except near the airfoil trailing edge. These results demonstrate that the present code and turbulence model can predict the flowfield about an airfoil with a large pressure jump (shock wave) and trailing-edge separation. The disagreement in the small separated region near the trailing edge is again attributed to inadequate turbulence modeling in this region.

A careful examination of the present computer code revealed one obvious coding error which introduced a large numerical asymmetry and two subtle coding errors that *possibly* may introduce small numerical asymmetries. The computer code was corrected for the coding error which had introduced the large numerical asymmetry, the present unsteady-flow case was re-run, and essentially the same unsteady-flow solution was obtained. Correcting the code for the two subtle coding errors has proven more time consuming than originally anticipated. Since eliminating the possible sources of small numerical asymmetries should not alter the qualitative aspects of the agreement with experiment, the computed results obtained to date are being published without delay.

Even though there is strong circumstantial evidence that the present computed unsteady-flow results qualitatively reproduce the physical features of similar real flows, until similar results are obtained with a computer code with no numerical asymmetries, the present computed unsteady-flow results should be considered preliminary.

## IV. Concluding Remarks

A successful initial effort has been made in including wall boundary conditions in a computer code for solving the two-dimensional, compressible Navier-Stokes equations for flow over airfoils, albeit slip-flow wall boundary conditions were used. While inclusion of the wall boundary conditions does provide improved agreement with experimental results, it does not alter the conclusion of earlier investigators that improved turbulence models are required before existing codes can correctly predict the flow features characteristic of strong shock-wave boundary-layer interactions with relatively large regions of separated flow. Present results indicate that, with the availability of computer codes with proper boundary conditions, an improved tool is now in hand for quantitatively testing different kinds of turbulence models against data from two-dimensional, fully documented experiments.

Evidence is also in hand which shows (for the first time to the author's knowledge) that Navier-Stokes type computer codes are capable of reproducing the time-dependent aspects of unsteady turbulent flows involving weak and strong shock-wave boundary-layer interactions. Present computed results indicate that the intensity of airfoil surface-pressure and skin-friction fluctuations, the reduced frequency of pressure fluctuations, oscillatory regions of trailing-edge and shock-induced separation, and the Mach number range for unsteady flows can be qualitatively reproduced. These results inspire confidence that once turbulence models are developed with which the improved computer codes can predict experimental steady-flow results, the codes can then be used to study the time-dependent aspects of unsteady flows and hence provide insight into unsteady aerodynamic phenomena such as buffeting, inlet buzz, and rotating helicopter blades.

## References

[1] Marvin, J. G., "Experiments Planned Specifically for Developing Turbulence Models in Computations of Flow Fields Around Aerodynamic Shapes," AGARD-CP-210, Oct. 1976.

[2] McDevitt, J. B., Levy, L. L. Jr. and Deiwert, G. S., "Transonic Flow About a Thick Circular-Arc Airfoil," *AIAA Journal*, Vol. 14, May 1976, pp. 606-613.

[3] Rubesin, M. W., Okuno, A. F., Levy, L. L. Jr., McDevitt, J. B., and Seegmiller, H. L., "An Experimental and Computational Investigation of the Flow Field About a Transonic Airfoil in Supercritical Flow with Turbulent Boundary-Layer Separation," 10th Congress of the International Council of the Aeronautical Sciences, Ottawa, Canada, Oct. 4-8, 1976; also NASA TM X-73,157, July 1976.

[4] Deiwert, G. S., "Computation of Separated Transonic Turbulent Flows," AIAA paper 75-829, Hartford, Conn., June 1975.

[5] Deiwert, G. S., "On the Prediction of Viscous Phenomena in Trankonic Flows," Project SQUID Workshop on Transonic Flow Problems in Turbomachinery, Monterey, Calif., Feb. 1975.

[6] Deiwert, G. S., "Numerical Simulation of High Reynolds Number Transonic Flows," *AIAA Journal*, Vol. 13, Oct. 1975, pp. 1354-1359.

[7]Deiwert, G. S., "High Reynolds Number Transonic Flow Simulation," *Lecture Notes in Physics*, Vol. edited by Springer-Verlag, 1975, p. 132.

[8]Baldwin, B. S., MacCormack, R. W., and Deiwert, G. S., "Numerical Techniques for the Solution of the Compressible Navier-Stokes Equations and Implementation of Turbulence Models," AGARD-LSP-73, March 1975.

[9]MacCormack, R. W., "An Efficient Numerical Method for Solving the Time-Dependent Compressible Navier Stokes Equations at High Reynolds Number," NASA TM X-73,129, July 1976.

[10]Seegmiller, H. L., Marvin, J. G., and Levy, L. L. Jr., "Steady and Unsteady Transonic Flow," AIAA Paper 78-160, Huntsville, Ala., Jan. 1978.

[11]Polentz, P. P., Page, W. A., and Levy, L. L., Jr., "Unsteady Normal-Force Characteristic of Selected NACA Profiles at High Subsonic Mach Numbers," NACA RM A55C02, May 1955.

[12]Finke, K., "Unsteady Shock-Wave Boundary-Layer Interaction on Profiles in Transonic Flow," AGARD-CPP-168, Paper 28, May 1975.

[13]McDevitt, J. B., Private communication on NASA Ames experiment, 1977.